

# Metal Saturation and the Redistribution of Hydrogen in Earth's Mantle

Junjie Dong<sup>a,b,\*</sup>, Lars P Stixrude<sup>c</sup>, Paul D Asimow<sup>a</sup>, Jie Li<sup>d</sup>

<sup>a</sup>*Division of Geological and Planetary Sciences, California Institute of Technology, Pasadena, CA 91125, USA*

<sup>b</sup>*Department of Geosciences, State University of New York at Stony Brook, Stony Brook, NY 11794, USA*

<sup>c</sup>*Department of Earth, Planetary, and Space Sciences, University of California, Los Angeles, CA 90095, USA*

<sup>d</sup>*Department of Earth and Environmental Sciences, University of Michigan, Ann Arbor, MI 48109, USA*

---

## Abstract

Iron disproportionation reactions in mantle silicates can produce metallic iron that drives Earth's deep mantle toward metal saturation under reduced conditions. Subducting slabs transport hydrated silicates to these depths, where interactions with metallic iron can reduce structurally bound hydrogen in silicates to reduced hydrogen-bearing phases, such as molecular hydrogen or iron hydrides, leaving mantle rocks in effect dry. Using the thermodynamic code HeFESTo with its latest self-consistent treatment of iron-bearing mantle phases, we investigate the stability and distribution of metallic iron in Earth's pyrolytic mantle across a broad range of oxidation states, represented by whole-rock  $\text{Fe}^{3+}/\Sigma\text{Fe}$  ratio from 1% to 10%. We find that metallic iron is present through much of the lower mantle across this range and, under very reduced compositions of whole-rock  $\text{Fe}^{3+}/\Sigma\text{Fe} = 1\text{--}3\%$ , extends into the upper mantle. Where subducted water meets metal-saturated regions, hydrous melts may form and migrate upward, rehydrating the overlying mantle or pooling near the transition zone. Metal saturation can thus redistribute hydrogen internally, creating a sharp contrast between a wet shallow mantle and a dry deep mantle. This redox-driven redistribution can decrease mantle silicate water storage capacity by 64–96% today, to only 0.1–0.8 modern ocean masses, and may explain the viscosity contrast near the upper–lower mantle boundary. Although quantitative estimates of metal abundance and distribution depend on thermodynamic assumptions and remain uncertain above 50 GPa, our results reveal the role of redox reactions between disproportionated iron and subducted water in governing the speciation and redistribution of hydrogen in Earth's mantle.

*Keywords:* Iron disproportionation, Metal saturation, Mantle oxidation state, Mantle hydrogen, Deep water cycle, Thermodynamic modeling

---

## 1. Introduction

Water on Earth's surface sustains its habitability over geological timescales. The abundance of surface water is regulated by fluxes in the deep water cycle between surface and interior, through volcanic outgassing and subduction recycling (*e.g.*, van Keken et al., 2011). In turn, the

---

\*Corresponding author

Email address: dong2j@caltech.edu (Junjie Dong)

abundance of interior water alters the vigor of mantle convection and thereby influences these fluxes, as variations in mantle water content regulate both the rate of volcanic outgassing and the efficiency of water retention during subduction (*e.g.*, Chotalia et al., 2020).

While the abundance of surface water can be measured precisely, the abundance of mantle water, an interior reservoir that directly interacts with the surface, cannot. Geochemical constraints come from surface rock samples such as basalts and xenoliths, but they reflect only shallow mantle source regions. Remote sensing through electrical conductivity and seismic properties provides geophysical constraints on in situ mantle water content, but interpretations remain ambiguous: temperature, composition, and deformation can all mimic the effect of water, and resolution decreases with depth (*e.g.*, Khan, 2016).

Laboratory measurements and thermodynamic modeling of structurally bound hydrogen (OH) solubility in the nominally anhydrous minerals (NAMs) within the ambient mantle can provide a theoretical upper bound for the bulk mantle water content, but reliable data are largely limited to upper mantle and transition zone minerals (*e.g.*, Dong et al., 2021). For the lower mantle, available experimental data are scarce and inconsistent, often limited to the topmost lower mantle conditions (25–27 GPa), and scatter widely (*e.g.*, Panero et al., 2015; Fu et al., 2019; Liu et al., 2021; Lu et al., 2025), ranging from nearly zero to a few thousand ppm by weight in bridgmanite, its most abundant mineral. As a result, both the form and abundance of water in the lower mantle, which makes up roughly half of Earth’s mass, remain largely unresolved.

Most existing experimental constraints on water-hosting mantle phases, from NAMs and hydrous minerals to hydrous melts, have been obtained in compositions more oxidized than those expected for Earth’s lower mantle. Compared with the shallow upper mantle, which has oxygen fugacity ( $f_{O_2}$ ) near the fayalite–magnetite–quartz (FMQ) buffer, the deep mantle is far more reduced, extending below the iron–wüstite (IW) buffer (after Frost et al., 2004; McCammon, 2005a; Frost and McCammon, 2008). This reduced condition is imposed by the precipitation of metallic iron ( $Fe^0$ ), produced by charge disproportionation of ferrous iron in mantle silicates. Such disproportionation reactions have been experimentally characterized in bridgmanite across lower mantle compositions (Frost et al., 2004; Huang et al., 2021a,b; Wang et al., 2023, 2025), and in clinopyroxene and garnet in the deep upper mantle and transition zone under reduced compositions (Rohrbach et al., 2007; Beyer et al., 2021).

Once formed, disproportionated metal reacts with water-hosting phases typical of the oxidized shallow mantle, removing oxygen-bound hydrogen from NAMs, hydrous minerals, and melts, and forming reduced species such as molten iron hydride ( $FeH_x$ ) and molecular hydrogen ( $H_2$ ) fluid (Yagi and Hishinuma, 1995; Okuchi, 1997; Shibazaki et al., 2009; Iizuka-Oku et al., 2017; Yuan et al., 2018; Zhu et al., 2019; Iizuka-Oku et al., 2021; Kim et al., 2023; Zhu et al., 2025a,b). These iron–water reactions imply a fundamental dichotomy in mantle water distribution: in the metal-free shallow mantle, water is stored primarily as structural OH within the NAMs, together with hydrous minerals and melts carried by cold slabs; in contrast, the metal-saturated deep mantle disproportionates water, creating dry, oxidized rocks and modally minor, reduced hydrogen-bearing phases such as  $H_2$  and molten  $FeH_x$ . These reduced hydrogen-bearing phases may migrate upward, rehydrating the overlying mantle and leaving the mantle rocks in the metal-saturated regions effectively dry. The transition from hydrated to dry silicates is ultimately controlled by the depth at which metal saturation is attained.

Despite the widespread occurrence of metal in the deep mantle, its role in the deep water cycle has not been systematically considered. Here, we investigate the distribution and abundance of metallic  $Fe^0$  in Earth’s mantle and evaluate its role in governing the speciation and distribution of water across the full range of plausible mantle potential temperatures and oxidation states.

We then discuss the geophysical implications, suggesting that hydrous melts responsible for seismic low-velocity zones near the transition zone may result from reactions between subducted water and the metal-saturated deep mantle, and that the viscosity contrast between the upper and lower mantle reflects hydrolytic weakening in the wet shallow mantle and its absence in the dry deep mantle. Our results are based on thermodynamic modeling and are therefore subject to uncertainties in experimental constraints on the ferric content of mantle minerals and in the choice of equations of state, particularly at lower mantle pressures; accordingly, we emphasize the robust qualitative trend in the prevalence of metallic iron in much of Earth’s lower mantle over geologic time, and discuss how its role in hydrogen redistribution can be further tested by experiments.

## 2. Methods

### 2.1. Iron disproportionation in ferric iron-bearing minerals.

We used the thermodynamic code HeFESTo (Stixrude and Lithgow-Bertelloni, 2005, 2011, 2024a,b) to compute the stable mineral assemblages of a pyrolitic mantle, including the abundance and distribution of metallic Fe<sup>0</sup> produced by disproportionation reactions. All calculations were based on the latest self-consistent parameter set, which incorporates the physics of iron-bearing mantle-related species (Stixrude and Lithgow-Bertelloni, 2024a,b).

Six ferric Fe<sup>3+</sup> species were considered across five mantle silicate minerals that involving charge disproportionation of iron:

1. magnetite (Fe<sup>2+</sup>Fe<sup>3+</sup>Fe<sup>3+</sup>O<sub>4</sub>) in spinel (*sp*),
2. acmite (Na<sup>+</sup>Fe<sup>3+</sup>Si<sup>4+</sup><sub>2</sub>O<sub>6</sub>) in clinopyroxene (*cpx*),
3. andradite (Ca<sup>2+</sup><sub>3</sub>Fe<sup>3+</sup>Fe<sup>3+</sup>Si<sup>4+</sup><sub>3</sub>O<sub>12</sub>) in garnet (*gt*),
4. the Fe<sup>3+</sup>Fe<sup>3+</sup>O<sub>3</sub> and Fe<sup>3+</sup>Al<sup>3+</sup>O<sub>3</sub> components in bridgmanite (*bg*) (Figure S1),
5. and the Fe<sup>3+</sup>Fe<sup>3+</sup>O<sub>3</sub> component in post-perovskite (*ppv*).

In previous versions of the HeFESTo code (Stixrude and Lithgow-Bertelloni, 2005, 2011), only ferrous Fe<sup>2+</sup> was considered, and oxygen content was not explicitly defined but inferred from the number of cations. This fixed amount of oxygen,  $b_{\text{O}}^*$ , was calculated as:

$$b_{\text{O}}^* = 2b_{\text{Si}} + b_{\text{Mg}} + b_{\text{Fe}} + b_{\text{Ca}} + 1.5b_{\text{Al}} + 0.5b_{\text{Na}} + 1.5b_{\text{Cr}}, \quad (1)$$

where all iron was assumed to be ferrous (Fe<sup>2+</sup>). When multiple valence states of iron are introduced in Stixrude and Lithgow-Bertelloni (2024a,b), the total amount of oxygen,  $b_{\text{O}}$ , becomes an independent variable and *no longer* equals  $b_{\text{O}}^*$ . It is instead determined by the whole-rock Fe<sup>3+</sup>/∑Fe ratio, defined as:

$$2(b_{\text{O}} - b_{\text{O}}^*)/b_{\text{Fe}}, \quad (2)$$

where  $b_{\text{O}}^*$  represents the amount of oxygen assuming all iron is ferrous, and  $b_{\text{Fe}}$  is the total iron content. Full details on the treatment of iron disproportionation and several benchmark cases against experimental data are provided in the Supplementary Material, Sections S1–S4 and Figures S1–S8.

We assume a well-mixed mantle with a pyrolitic model composition and vary its oxidation state by adjusting the whole-rock Fe<sup>3+</sup>/∑Fe ratio (Workman and Hart, 2005, Table S1 in Supplementary Material). The bulk composition of pyrolite was taken from Workman and Hart

(2005) and includes SiO<sub>2</sub>, MgO, FeO (total iron), CaO, Al<sub>2</sub>O<sub>3</sub>, Na<sub>2</sub>O, and Cr<sub>2</sub>O<sub>3</sub> (Table S1 in Supplementary Material). Estimates for various mantle rocks range from 2% (xenoliths) to 6% (MORB sources) (*e.g.*, McCammon, 2005b; Frost and McCammon, 2008; Hirschmann, 2023; Aulbach and Brounce, 2025, and references therein). We adopt a broader range of 1–10% for the whole-rock Fe<sup>3+</sup>/ΣFe ratio in the pyrolitic mantle, and 1–3% as the most likely present-day range (*e.g.*, Frost et al., 2004; Huang et al., 2021a; Wang et al., 2025). To approximate the geothermal gradients of a convecting mantle, we calculated isentropes of mantle assemblages for potential temperatures ( $T_p$ ) ranging from 1600 to 1900 K. This range covers the thermal states of the solid mantle from the present-day to the early Archean (*e.g.*, Herzberg et al., 2010).

## 2.2. Water solubility in nominally anhydrous minerals.

When the ambient mantle is metal-free, the nominally anhydrous minerals (NAMs) become available to host structurally bound OH (and the maximum as water solubility). The bulk water storage capacity of mantle rocks,  $c_{\text{H}_2\text{O}}^{\text{mantle}}$ , can be approximated, as an upper bound, by a weighted average (by their modal proportions  $X$ ) of the water solubilities of the NAM phases present,  $c_{\text{H}_2\text{O}}^{\text{NAM}}$  at each pressure ( $P$ ) and temperature ( $T$ ) (*e.g.*, Dong et al., 2022):

$$c_{\text{H}_2\text{O}}^{\text{mantle}} = \left( c_{\text{H}_2\text{O}}^{\text{NAM}} \right)_i \left( X_i + \sum_j X_j D_{\text{H}_2\text{O}}^{i/j} \right) \quad (3)$$

$D_{\text{H}_2\text{O}}^{i/j}$  is the partition coefficient of H<sub>2</sub>O between reference NAM phases  $i$ , including olivine, wadsleyite, ringwoodite, bridgmanite, and post-perovskite) and other modally minor phases  $j$  including orthopyroxene, clinopyroxene, high-pressure clinoenstatite, garnet, akimotoite, stishovite, davemaoite, and ferropericlase.

For minerals with well-characterized pressure- and temperature-dependent solubility (olivine, wadsleyite, ringwoodite), we applied parameterized fits to the experimental data of the following equation (Dong et al., 2021):

$$\ln(c_{\text{H}_2\text{O}}) = a + \frac{n}{2} \ln f_{\text{H}_2\text{O}}(P, T) + \frac{b + cP}{T} \quad (4)$$

Here,  $f_{\text{H}_2\text{O}}(P, T)$  is the water fugacity (GPa), and the constants  $a$ ,  $b$ , and  $c$  parameterize the entropy, enthalpy, and volume terms of the hydration reaction, respectively;  $n$  is the fugacity exponent. For the other phases, we used published partitioning coefficient of water relative to a reference NAM. Although the pressure–temperature dependence of water solubility in bridgmanite remains uncertain, our model is consistent with state-of-the-art experimental constraints with solubilities ranging from tens to hundreds of ppm by weight under oxidized conditions (*e.g.*, Fu et al., 2019; Liu et al., 2021; Lu et al., 2025). For details on the parameterization of NAM water solubility and data sources, see Dong et al. (2021, 2022).

## 3. Results and Discussion

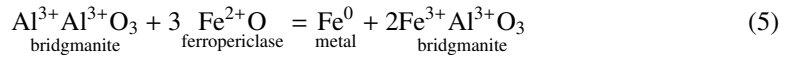
### 3.1. Effects of pressure and temperature on ferric content in mantle minerals under reduced conditions

To begin, we performed benchmark calculations against the available experimental constraints. We focus primarily on the effects of  $P$  and  $T$  on ferric content in mantle minerals in the reduced endmember of a pyrolitic mantle with a whole-rock Fe<sup>3+</sup>/ΣFe = 1%. Such a reduced

composition causes the mantle  $fO_2$  to stay at  $\Delta IW \approx -1$  anywhere deeper than 300 km and allows for the formation of metal from clinopyroxene, garnet and bridgmanite. This reduced endmember of pyrolite allows us to evaluate the performance of our model against experimental data collected under similarly reduced conditions, often imposed by metallic Fe buffers in multi-anvil (MA) experiments (e.g., Frost et al., 2004; Rohrbach et al., 2007; Stagno et al., 2011; Huang et al., 2021a).

Figures 1a and 1b show the  $P$ - $T$  effects on the ferric content of clinopyroxene and garnet at  $fO_2(\Delta IW) \approx -1$  within pyrolite. No temperature effect was found for clinopyroxene, while a slight positive effect was predicted for garnet. By plotting different isobars, we also isolate and show the pressure effects for clinopyroxene and garnet. A positive pressure effect is predicted for clinopyroxene. Garnet initially shows a positive effect that is then reversed and followed by a negative effect between 17 and 20 GPa. These predictions broadly align with the experimental data of Rohrbach et al. (2007); Beyer et al. (2021), though the effects are subtle and require further experimental validation. Compared to the amount of metallic  $Fe^0$  that could be produced by bridgmanite in the lower mantle, the contribution of clinopyroxene and garnet in the upper mantle and transition zone is relatively small and limited to very reduced compositions with low whole-rock  $Fe^{3+}/\Sigma Fe$  (Figures. 2–3). Therefore, we will primarily focus on bridgmanite, and a comprehensive analysis of clinopyroxene and garnet within pyrolite under varying  $P$ - $T$ - $X$  conditions shall be pursued elsewhere.

Two ferric  $Fe^{3+}$  species,  $Fe^{3+}Fe^{3+}O_3$  and  $Fe^{3+}Al^{3+}O_3$ , are considered for iron disproportionation in bridgmanite. The latter is the dominant contributor to metal production (Figure S7). At  $fO_2(\Delta IW) \approx -1$ , the ferric content of bridgmanite within pyrolite shows both negative temperature and negative pressure effects, agreeing well with the MA results at 25–27 GPa by Frost et al. (2004); Huang et al. (2021a) and aligned with our calculation of the Al-bearing bridgmanite with the simplified compositions (Figures. S3–S5). We highlight the negative pressure effect on bridgmanite that decreases metal production at greater depths using the isobars in Figure 1c. This trend results from the leftward shift of the following reaction:



with increasing pressure and is ultimately governed by the equations of state (EoS) chosen for the species involved. This choice is particularly critical, as the  $FeAlO_3$  has not been synthesized as a pure perovskite-structured phase, and its EoS is inferred from measurements of bridgmanite solid solutions, the extrapolation of which may carry large uncertainties. We follow the EoS choices in Stixrude and Lithgow-Bertelloni (2024b), supported by the results and analyses from Dorfman and Duffy (2014). This negative pressure effect for bridgmanite shown in Fig 1c is consistent with previous thermodynamic models of Al-bearing simplified systems that used independent choices of equations of state for different bridgmanite species (Huang et al., 2021b), which reinforces the reliability of this negative pressure trend despite the uncertainties from different equation-of-state choices.

Benchmarking our calculations against experimental data, particularly the negative pressure effect on bridgmanite within a reduced pyrolitic mantle at  $fO_2(\Delta IW) \approx -1$  above 25–27 GPa, remains difficult, primarily due to the scarcity of experimental constraints and their large uncertainties at lower mantle pressures. Almost all existing data relevant to lower mantle assemblages were collected under more oxidized conditions ( $fO_2(\Delta IW) > +1$ – $+2$ ; e.g., Piet et al. (2016); Wang et al. (2025)) than what would be expected for a metal-saturated pyrolitic mantle with  $fO_2(\Delta IW) \approx -1$ .

Wang et al. (2025) present the only set of MA experiments extending beyond 25–27 GPa and up to 50 GPa with well-characterized  $f_{O_2}$ . Although these experiments are not metal-saturated and were conducted at  $f_{O_2}$  closer to  $\Delta IW \approx +2$ , rather than  $\Delta IW \approx -1$ , they can nonetheless be used to indirectly benchmark our thermodynamic model. Our calculations performed using simplified compositions, pressures, and temperatures identical to those of Wang et al. (2025) show modest negative pressure effects on bridgmanite between 25 and 50 GPa, in excellent agreement with all experimental data reported in that study (Figures S4–S5). We emphasize that the pyrolitic composition adopted in Figure 1 is more complex than the simplified compositions often pursued experimentally (*e.g.*, Wang et al., 2025); pyrolite includes components such as CaO, Na<sub>2</sub>O, and Cr<sub>2</sub>O<sub>3</sub> and, for example, produces a realistic lower-mantle assemblage of bridgmanite, ferropericlase, and davemaolite, rather than simplified systems of (Fe, Al)-bearing bridgmanite with excess MgO or SiO<sub>2</sub> as is common in MA experiments (Frost et al., 2004; Huang et al., 2021a; Wang et al., 2023, 2025). A full benchmark comparison is provided in the Supplementary Material, where we calculated the effects of  $P$ – $T$ – $X$  on bridgmanite using simplified compositions identical to those employed in the MA experiments.

In our calculations, the negative pressure effect becomes more pronounced above  $\sim 80$  GPa. In the absence of MA experiments above 50 GPa with well-characterized  $f_{O_2}$ , we turn to diamond anvil cell (DAC) data for a semi-quantitative comparison. One DAC data point from Piet et al. (2016) shows a significantly lower ferric content in bridgmanite ( $19 \pm 3$  % at  $2400 \pm 100$  K and  $86 \pm 4$  GPa), which is below both their other measurements and the whole-rock  $Fe^{3+}/\Sigma Fe$  of the starting material ( $25 \pm 4$  %). Since bridgmanite is expected to host most of the ferric  $Fe^{3+}$  in lower mantle assemblages, its ferric content should exceed that of the bulk composition. This discrepancy suggests that the sample might have had more reduced conditions than originally reported, likely due to the open-system nature of DAC experiments, which do not use any redox buffer. We therefore include this reinterpreted data point in Figure 1c as an upper bound for a reduced pyrolitic composition near 80 GPa. Under this reinterpretation, the negative temperature effect for bridgmanite at  $f_{O_2}(\Delta IW) \approx -1$  that we predict can reasonably reproduce the data collected at  $86 \pm 4$  GPa) from Piet et al. (2016).

### 3.2. Metal distribution in Earth’s deep mantle today

With the thermodynamic model benchmarked against available experimental constraints, we now compute metal abundance in Earth’s mantle across redox states and time. Here, we demonstrate how oxidation state influences metal saturation in the present-day mantle by modeling the most oxidized and most reduced endmembers of a pyrolitic mantle (whole-rock  $Fe^{3+}/\Sigma Fe = 1$  and 10%), which bracket the likely present-day range of 1–3% (*e.g.*, Frost et al., 2004; Huang et al., 2021a; Wang et al., 2025). For each endmember, we compute phase proportions of mantle mineral assemblages as a function of pressure and depth (Figure 2) along an isentrope with  $T_p = 1600$  K.

For the reduced endmember (Figure 2a), metallic  $Fe^0$  is stable from the upper mantle down to the core–mantle boundary. Its abundance increases to approximately 0.1 wt% in the deep upper mantle and upper transition zone, where olivine and wadsleyite are predominant, and decreases to approximately 0.01–0.05 wt% in the lower transition zone dominated by ringwoodite. This reversal is driven by the negative pressure effect on the disproportionation reaction in majoritic garnet at the transition zone pressures (Figure 1b), where wadsleyite and ringwoodite (ferrous phases that coexist with garnet) favors resorption of metallic  $Fe^0$  into the silicates, converting  $Fe^{3+}$  and  $Fe^0$  back to  $Fe^{2+}$ . This trend aligns with recent experimental data on garnet in KLB-1 peridotite and is consistent with the thermodynamic model of Beyer et al. (2021). At the top of

the lower mantle, metallic  $\text{Fe}^0$  increases again, peaking at approximately 0.69 wt%, driven by disproportionation in bridgmanite. With increasing pressure, metal abundance decreases. Around 120 GPa, where bridgmanite transforms to post-perovskite, metallic  $\text{Fe}^0$  falls to approximately 0.05 wt%, with a similar amount subsequently produced by post-perovskite.

In contrast, in the oxidized endmember in Figure 2b, metallic  $\text{Fe}^0$  is not stable in the upper mantle or transition zone. Iron disproportionation occurs only in bridgmanite and is confined to the lower mantle, where  $\text{Fe}^0$  peaks at approximately 0.43 wt% near its top and diminishes with depth. It is fully resorbed into bridgmanite at about 75 GPa and 1750 km. This stronger negative pressure effect is consistent with behavior predicted for more oxidized compositions (Figure S7) and is supported by the similar pressure dependence observed in simplified systems of bridgmanite with excess MgO (Figure S3–5).

We compare these modeled endmembers with natural constraints, shown in Figure 2. The ferric  $\text{Fe}^{3+}$  content of majoritic garnet in diamond inclusions (Kiseeva et al., 2018), falls between our two endmember predictions. Likewise, the  $f_{\text{O}_2}$  values derived from Udachnaya mantle xenoliths (Miller et al., 2016) align with our modeled range at pressures above 10 GPa, where the mantle geotherm becomes nearly adiabatic.

### 3.3. Persistent metal saturation across redox states and time

To evaluate the prevalence of metal saturation and its systematic variation with mantle oxidation state over geological time, we extend our calculations across the full plausible range of mantle oxidation states, from whole-rock  $\text{Fe}^{3+}/\Sigma\text{Fe} = 1\%$  to 10%, spanning the geological history of Earth’s mantle since its solidification with mantle  $T_p = 1600$  K (present day) to 1900 K (Archean). Our results show that metallic  $\text{Fe}^0$  is widespread in the deep mantle across these ranges (Figure 3) with its abundance and depth distribution depend on both whole-rock  $\text{Fe}^{3+}/\Sigma\text{Fe}$  and  $T_p$  (Figure 4).

Mantle oxidation state, represented by the whole-rock  $\text{Fe}^{3+}/\Sigma\text{Fe}$  ratio, exerts the strongest control; more reduced mantles (i.e. lower whole-rock  $\text{Fe}^{3+}/\Sigma\text{Fe}$ ) produce greater total metal mass (Table S2 in Supplementary Material; Figure 4a). At the present-day  $T_p$  of 1600 K and whole-rock  $\text{Fe}^{3+}/\Sigma\text{Fe}$  of 1–3%, the total metal mass is about  $8.6\text{--}10.5 \times 10^{21}$  kg (2120–2600 ppm by weight); under the same  $T_p$ , but much more oxidized mantles (6–10%, higher than present-day estimates), the total mass declines to about  $4.0\text{--}5.1 \times 10^{21}$  kg (990–1260 ppm by weight). Oxidation state not only controls the total metal mass but also shift the depths at which metal saturation is attained. At constant  $T_p$ , more reduced mantles reach metal saturation at shallower depths (Figure 4b). Under the assumption of a homogeneous mantle well mixed in whole-rock  $\text{Fe}^{3+}/\Sigma\text{Fe}$ , the combined negative dependence of pressure and temperature on bridgmanite lead to decreasing metal abundance with depth. The present-day mantle (1600 K, 1–3%) is still likely to remain metal-saturated close to the core–mantle boundary. By contrast, more oxidized mantles than previously estimated develop a metal-free zone just above the core, leaving the mantle in disequilibrium with it. In reality, redox heterogeneity or stratification may drive the lowermost mantle closer to equilibrium with the core at the core–mantle boundary (CMB) (Otsuka and Karato, 2012; Henningsen et al., 2025), a boundary layer we have not modeled.

Although less influential than mantle oxidation state, mantle  $T_p$  affects the depth and extent of metal saturation by simultaneously raising or decreasing pressure and temperature. Assuming constant whole-rock  $\text{Fe}^{3+}/\Sigma\text{Fe}$ , secular cooling of the mantle from  $T_p = 1900$  K to 1600 K increases total metal mass from 7 to  $9.5 \times 10^{21}$  kg, raising the whole-mantle concentration from 1750 to 2340 ppm by weight. This increase is largely driven by the negative temperature dependence on iron disproportionation in bridgmanite (Figure 1c; i.e. metal production from

bridgmanite decreases with increasing temperature). Majoritic garnet, responsible for metal production in the upper mantle and transition zone, has a positive temperature dependence (Figure 1b) opposite to that of bridgmanite (Figure 1c). Because bridgmanite dominates mantle mass, its negative temperature dependence tends to outweigh the positive temperature dependence of garnet, leading to a net decrease in whole-mantle metal abundance with higher  $T_p$ .

## 4. Implications

### 4.1. A dichotomy between wet shallow mantle and dry deep mantle

Water reservoirs in Earth’s mantle are conventionally understood to be dominated by structural water in NAMs and hydrous minerals, which can store substantial amounts of structurally bound OH under oxidized conditions near the FMQ buffer, for example, up to 2–3% by weight in wadsleyite and ringwoodite in the transition zone (*e.g.*, Dong et al., 2021). Bridgmanite, the most abundant mineral in Earth’s interior and the dominant phase of the lower mantle, may also incorporate water, but reported measurements of its water solubility range widely, from nearly zero to several thousand ppm by weight (*e.g.*, Panero et al., 2015; Fu et al., 2019; Liu et al., 2021; Lu et al., 2025). Assuming that all water is stored as structural OH in NAMs, including bridgmanite in the lower mantle, and that there are only negligible amounts of hydrous minerals due to their limited stability in the ambient mantle (*e.g.*, Yuan et al., 2019), Dong et al. (2021) placed the maximum size of mantle water reservoirs at approximately 2.3 modern ocean masses (OM, where 1 OM =  $1.335 \times 10^{21}$  kg) for the present-day mantle. This estimate is significantly reduced to 0.9 OM for a hotter early Archean mantle ( $T_p = 1900$  K).

However, such models presuppose a metal-free mantle and so exclude the effect of metal saturation formed from iron disproportionation, which becomes critical in Earth’s deep mantle: unlike the relatively oxidized shallow mantle within log units of the FMQ buffer, the widespread occurrence of metallic  $\text{Fe}^0$  imposes far more reduced conditions near the IW buffer and reacts with and consumes oxygen-bound hydrogen from NAMs, fundamentally redistributing water in the deep mantle. Experimental studies have consistently shown that, under mantle conditions, disproportionated metal can dehydrate water-hosting phases, including NAMs such as ringwoodite and wadsleyite (Shibazaki et al., 2009; Zhu et al., 2019), hydrous minerals such as brucite (Iizuka-Oku et al., 2017, 2021; Kim et al., 2023; Zhu et al., 2025a) and superhydrous phases B, E, and Egg (Zhu et al., 2025a), as well as hydrous melt and free water (Okuchi, 1997; Yuan et al., 2018), producing molten  $\text{FeH}_x$  (Yagi and Hishinuma, 1995; Iizuka-Oku et al., 2021; Zhu et al., 2025a,b) or molecular  $\text{H}_2$  fluid (Iizuka-Oku et al., 2017; Zhu et al., 2025a). These iron–water reactions take place at the margins of metal saturation in the deep mantle, which act as an “iron wringer” that extracts oxygen-bound hydrogen and prevents hydration of adjacent mantle rocks (Figure 3b). Much of the deep mantle is then left dry in most modeled scenarios, despite having mineral assemblages with high intrinsic bulk water storage capacity under oxidized conditions.

As opposed to earlier models that considered only water solubility in NAMs (*e.g.*, Dong et al., 2021), we explicitly account for the presence of disproportionated metal. Using the modeled metal abundance and distribution as a function of mantle  $T_p$  and whole-rock  $\text{Fe}^{3+}/\Sigma\text{Fe}$  (Figure 3a), we evaluate the location of hydratable NAMs under oxidized mantle conditions and their bulk water storage capacity, excluding all reduced, metal-saturated zones (Figure 3b; Section S5 in Supplementary Material). The results show that at present mantle conditions (1600 K, 1–3%), relative to the metal-free model, the whole-mantle water capacity falls sharply by about 90%, from 2.3 OM to 0.1–0.8 OM. For mantles far more oxidized than present-day estimates

(6–10%), this decrease is more modest at about 20%. This notable contrast arises because, at low whole-rock  $\text{Fe}^{3+}/\Sigma\text{Fe}$  ratios, metal saturation extends up into the transition zone and even the upper mantle, preventing hydration in the region with the highest intrinsic water storage capacity when metal-free. At higher whole-rock  $\text{Fe}^{3+}/\Sigma\text{Fe}$  ratios, however, metal saturation remains largely confined to the lower mantle, thereby preserving significant bulk water storage capacity in the transition zone. Overall, depending on mantle  $T_p$  and whole-rock  $\text{Fe}^{3+}/\Sigma\text{Fe}$  ratio, the whole-mantle water storage capacity decreases from 0.7–2.3 to 0.1–1.9 OM, contracting by 18–96% once metallic  $\text{Fe}^0$  from iron disproportionation is taken into account (Figure 5; Table S3 in Supplementary Material).

Figure 3b shows how water storage capacity in NAMs varies with depth in relation to metal saturation. In the upper mantle at 10 GPa, NAMs can retain about 470 ppm water by weight, owing to the absence of metallic  $\text{Fe}^0$  at this depth. In the transition zone at 20 GPa, metal saturation eliminates water storage in NAMs under reduced bulk compositions (1–3%), whereas under much more oxidized bulk compositions (6–10%), NAMs retain a high water storage capacity (about 3900 ppm by weight). As shown in Figure 3a, in the lowermost mantle between 80 and 120 GPa, our model predicts the loss of metal saturation, once again allowing moderate water storage of about 290 ppm by weight in bridgmanite. Our prediction is consistent with experimental observations: recent laser-heated diamond anvil cells experiments by Zhang et al. (2024) show that with 2% water by weight, bridgmanite coexists with metallic  $\text{Fe}^0$  at 90 GPa but becomes metal-free above 105–108 GPa.

Alternative choices of equations of state for bridgmanite, as discussed in Section 3.1, can allow metal saturation to extend all the way to the CMB at more oxidized bulk compositions than the whole-rock  $\text{Fe}^{3+}/\Sigma\text{Fe}$  ratio used here (Huang et al., 2021b; Wang et al., 2025), eliminating any hydration of silicates at depth. The precise extent of metal saturation in the lowermost mantle remains to be tested experimentally; however, a weaker negative pressure effect does not negate, and may in fact reinforce, our central conclusion: for a wide range of plausible whole-rock  $\text{Fe}^{3+}/\Sigma\text{Fe}$  ratios, most of the deep mantle is predicted to have been metal-saturated throughout Earth’s history and, by extension, the metal-saturated lower mantle today likely contains only a negligible amount of structural OH. This reflects not the intrinsic water solubility in bridgmanite, if any under oxidized conditions (*e.g.*, Fu et al., 2019; Liu et al., 2021; Lu et al., 2025), but rather the incompatibility of its structural OH with disproportionated metal (*e.g.*, Zhu et al., 2019).

#### 4.2. Redistribution of hydrogen in Earth’s deep mantle and its geophysical consequences

The final consideration is the consequences of iron–water reactions, which are expected to occur when subducting slabs deliver water-hosting phases into contact with metal-saturated deep mantle, and when ascending ambient mantle rises out of metal saturation into the oxidized shallow mantle. Experiments show that molecular  $\text{H}_2$  fluid and molten  $\text{FeH}_x$  are the two main hydrogen-bearing reaction products, with the dominant phase depending on whether water is in excess or metal is in excess (endmember reaction with excess water:  $2\text{Fe} + 3\text{H}_2\text{O} \rightleftharpoons \text{Fe}_2\text{O}_3 + 3\text{H}_2$ ; endmember reaction with excess metal:  $(1 + \frac{2}{x})\text{Fe} + \text{H}_2\text{O} \rightleftharpoons \text{FeO} + \frac{2}{x}\text{FeH}_x$ ) (Zhu et al., 2019). We infer that these same reactions also govern mantle-scale iron–water interactions. In Earth’s mantle, the likelihood of these two endmember reactions varies spatially and temporally. Regions dominated by sustained subduction and accumulation of hydrated slabs may locally reach water-excess conditions, favoring the production and rapid upward migration of  $\text{H}_2$  fluid. Conversely,  $\text{FeH}_x$  may form as the dominant reaction product when metal-saturated, deep-mantle assemblages ascend passively into shallower, more oxidized regions.  $\text{FeH}_x$  is unlikely to form

an interconnected network in the silicate matrix and sink, given its extremely small modal abundance (von Bagen and Waff, 1986) and high interfacial tension with silicates (Hishinuma et al., 1994), therefore it is expected to be trapped within reduced rock assemblages (Zhang et al., 2016). Upon gradual ascent into shallower depths, any  $\text{FeH}_x$  present in the rock assemblages would quickly destabilize as the ambient mantle  $f_{\text{O}_2}$  rises above the IW buffer (Figure S10–S11 in Supplementary Material) and Fe and  $\text{H}_2$  become immiscible at shallow conditions (e.g., Stoutenburg et al., 2026).

The upward flux of either  $\text{H}_2$  or  $\text{FeH}_x$  has the potential to generate hydrous melts and rehydrate NAMs in the overlying mantle (e.g., Hirschmann et al., 2012; Yang et al., 2016; Yang, 2016; Moine et al., 2020; Zhu et al., 2025a), assuming that  $\text{H}_2$  is oxidized before it can outgas to the atmosphere, as suggested by experimental constraints (e.g., Kohlstedt and Mackwell, 1998; McCammon et al., 2004; Liu and Yang, 2020). Therefore, we propose that iron–water reactions primarily redistribute water internally within the mantle, resulting in water ultimately being stored in NAMs within the shallow, oxidized, metal-free region, leaving much of the deep mantle dry. Iron-rich hydrous melts produced by iron–water reactions may pond at 410 km and 660 km depths (e.g., Huang et al., 2023), depending on where metal saturation is encountered and neutral buoyancy is reached. These melts are consistent with seismic observations of low shear velocities at multiple locations and depths (e.g., Carr et al., 2025). Such features have been attributed to the “water-filter” model (Bercovici and Karato, 2003), in which large contrasts in bulk water storage capacity across mantle silicates drive melt formation. Our model suggests an alternative: in the presence of metallic  $\text{Fe}^0$ , silicate water solubility becomes effectively negligible, and hydrous melts can instead be generated by metal saturation as an “iron wringer”. Both models seek to explain seismic low-velocity zones, but where the “water-filter” model emphasizes solubility contrasts among silicates, our “iron wringer” model emphasizes the reactive role of metallic iron.

Regardless of which reduced, hydrogen-bearing phase is dominant, our model reveals a sharp transition in the distribution of mantle water (or more precisely hydrogen) across the upper–lower mantle boundary: from a wet, shallow mantle above to a dry, deep mantle below. Such a non-uniform distribution of hydrated rocks could strongly influence the mantle viscosity profile. Observations indicate that the deep mantle viscosity is a factor of 30–100 higher than that in the shallow mantle (after Peltier, 1985), with the transition likely occurring between the base of the upper mantle and the uppermost lower mantle. This dichotomy in water distribution offers a plausible explanation: in the shallow mantle, oxygen-bound hydrogen stored in NAMs significantly weakens silicates (e.g., Muir and Brodholt, 2018), whereas in the deep mantle structural water is absent, with little hydrolytic weakening effect on silicates to first order. The widespread metal saturation in the deep mantle likely helps sustain this viscosity contrast by exerting strong redox control over where hydrated silicates can form, thus maintaining long-term non-uniform distribution in mantle hydrogen.

## 5. Conclusions and Outlook

Our thermodynamic modeling suggests that metallic iron, produced by iron disproportionation reactions, is present in much of Earth’s deep mantle, from the Archean to the present, and across a broad range of oxidation states. Although the absolute abundance and exact depth distribution of this metal are sensitive to thermodynamic assumptions and experimental constraints, the predicted persistence of this exquisitely small amount of metal could govern the speciation and redistribution of hydrogen in the mantle. We therefore propose reframing the deep water

cycle as a problem severely constrained by redox reactions rather than solely by water solubility in mantle minerals. We suggest that interactions between subducted water and disproportionated iron can redistribute hydrogen within the mantle internally, potentially producing sharp contrasts in water storage and, by extension, in rock rheology between the metal-free and metal-saturated regions. In this conceptual framework, hydrogen is preferentially retained in the shallow, more oxidized mantle, while the deeper mantle having little to no ability to host structural OH in its silicates, even though the total amount of water or hydrogen in Earth's mantle remains unchanged in bulk.

Quantitative estimates at pressures above ~50 GPa remain uncertain because the magnitude, and even the sign, of the combined pressure and temperature effects on metal saturation depends on the choice of equations of state for bridgmanite (Huang et al., 2021b; Stixrude and Lithgow-Bertelloni, 2024b; Wang et al., 2025). Improved constraints will require advances in redox-buffered experiments and precise chemical analyses under lower mantle conditions. While this uncertainty complicates quantitative estimates, it does not negate the persistence of metallic Fe<sup>0</sup> through much of the deep mantle over geological time, with profound implications for the coupling between mantle redox state and the deep water cycle.

## References

- Aulbach, S., Brounce, M., 2025. Mantle redox, in: *Treatise on Geochemistry*. Elsevier, pp. 275–332. doi:10.1016/B978-0-323-99762-1.00101-7.
- von Bagen, N., Waff, H.S., 1986. Permeabilities, interfacial areas and curvatures of partially molten systems: Results of numerical computations of equilibrium microstructures. *Journal of Geophysical Research: Solid Earth* 91, 9261–9276. doi:10.1029/JB091iB09p09261.
- Bercovici, D., Karato, S.i., 2003. Whole-mantle convection and the transition-zone water filter. *Nature* 425, 39–44. doi:10.1038/nature01918.
- Beyer, C., Myhill, R., Marquardt, K., McCammon, C.A., 2021. A reversed redox gradient in Earth's mantle transition zone. *Earth and Planetary Science Letters* 575, 117181. doi:10.1016/j.epsl.2021.117181.
- Carr, S.A., Olugboji, T., Park, J., Karato, S.i., 2025. High-resolution mapping of North America suggests numerous low-velocity zones above and below the mantle transition zone. *Tectonophysics* 908, 230775. doi:10.1016/j.tecto.2025.230775.
- Chotalia, K., Cagney, N., Lithgow-Bertelloni, C., Brodholt, J., 2020. The coupled effects of mantle mixing and a water-dependent viscosity on the surface ocean. *Earth and Planetary Science Letters* 530, 115881. doi:10.1016/j.epsl.2019.115881.
- Dong, J., Fischer, R.A., Stixrude, L.P., Lithgow-Bertelloni, C.R., Eriksen, Z.T., Brennan, M.C., 2022. Water storage capacity of the martian mantle through time. *Icarus* 385, 115113. doi:10.1016/j.icarus.2022.115113.
- Dong, J., Fischer, R.A., Stixrude, L.P., Lithgow-Bertelloni, C.R., 2021. Constraining the Volume of Earth's Early Oceans With a Temperature-Dependent Mantle Water Storage Capacity Model. *AGU Advances* 2, e2020AV000323. doi:10.1029/2020AV000323.

- Dorfman, S., Duffy, T., 2014. Effect of Fe-enrichment on seismic properties of perovskite and post-perovskite in the deep lower mantle. *Geophysical Journal International* 197, 910–919. doi:10.1093/gji/ggu045.
- Frost, D.J., Liebske, C., Langenhorst, F., McCammon, C.A., Trønnes, R.G., Rubie, D.C., 2004. Experimental evidence for the existence of iron-rich metal in the Earth's lower mantle. *Nature* 428, 409–412. doi:10.1038/nature02413.
- Frost, D.J., McCammon, C.A., 2008. The Redox State of Earth's Mantle. *Annual Review of Earth and Planetary Sciences* 36, 389–420. doi:10.1146/annurev.earth.36.031207.124322.
- Fu, S., Yang, J., Karato, S., Vasiliev, A., Presniakov, M.Y., Gavriliuk, A.G., Ivanova, A.G., Hauri, E.H., Okuchi, T., Purevjav, N., Lin, J., 2019. Water Concentration in Single-Crystal (Al,Fe)-Bearing Bridgmanite Grown From the Hydrous Melt: Implications for Dehydration Melting at the Topmost Lower Mantle. *Geophysical Research Letters* 46, 10346–10357. doi:10.1029/2019GL084630.
- Henningsen, E.L., Korenaga, J., Marchi, S., 2025. Impact-Driven Redox Stratification of Earth's Mantle. *Journal of Geophysical Research: Solid Earth* 130, e2024JB030817. doi:10.1029/2024JB030817.
- Herzberg, C., Condie, K., Korenaga, J., 2010. Thermal history of the Earth and its petrological expression. *Earth and Planetary Science Letters* 292, 79–88. doi:10.1016/j.epsl.2010.01.022.
- Hirschmann, M., Withers, A., Ardia, P., Foley, N., 2012. Solubility of molecular hydrogen in silicate melts and consequences for volatile evolution of terrestrial planets. *Earth and Planetary Science Letters* 345-348, 38–48. doi:10.1016/j.epsl.2012.06.031.
- Hirschmann, M.M., 2023. The deep Earth oxygen cycle: Mass balance considerations on the origin and evolution of mantle and surface oxidative reservoirs. *Earth and Planetary Science Letters* 619, 118311. doi:10.1016/j.epsl.2023.118311.
- Hishinuma, T., Magi, T., Uchida, T., 1994. Surface Tension of Iron Hydride Formed by the Reaction of Iron-Silicate-Water under Pressure. *Proceedings of the Japan Academy, Series B* 70, 71–76. doi:10.2183/pjab.70.71.
- Huang, R., Boffa Ballaran, T., McCammon, C.A., Frost, D.J., 2023. The composition and redox state of hydrous partial melts generated at the top of the lower mantle. *Earth and Planetary Science Letters* 624, 118447. doi:10.1016/j.epsl.2023.118447.
- Huang, R., Boffa Ballaran, T., McCammon, C.A., Miyajima, N., Dolejš, D., Frost, D.J., 2021a. The composition and redox state of bridgmanite in the lower mantle as a function of oxygen fugacity. *Geochimica et Cosmochimica Acta* 303, 110–136. doi:10.1016/j.gca.2021.02.036.
- Huang, R., Boffa Ballaran, T., McCammon, C.A., Miyajima, N., Frost, D.J., 2021b. The Effect of Fe-Al Substitution on the Crystal Structure of MgSiO<sub>3</sub> Bridgmanite. *Journal of Geophysical Research: Solid Earth* 126, e2021JB021936. doi:10.1029/2021JB021936.

- Iizuka-Oku, R., Gotou, H., Shito, C., Fukuyama, K., Mori, Y., Hattori, T., Sano-Furukawa, A., Funakoshi, K.i., Kagi, H., 2021. Behavior of light elements in iron-silicate-water-sulfur system during early Earth's evolution. *Scientific Reports* 11, 12632. doi:10.1038/s41598-021-91801-3.
- Iizuka-Oku, R., Yagi, T., Gotou, H., Okuchi, T., Hattori, T., Sano-Furukawa, A., 2017. Hydrogenation of iron in the early stage of Earth's evolution. *Nature Communications* 8, 14096. doi:10.1038/ncomms14096.
- van Keken, P.E., Hacker, B.R., Syracuse, E.M., Abers, G.A., 2011. Subduction factory: 4. Depth-dependent flux of H<sub>2</sub> O from subducting slabs worldwide. *Journal of Geophysical Research* 116, B01401. doi:10.1029/2010JB007922.
- Khan, A., 2016. On Earth's Mantle Constitution and Structure from Joint Analysis of Geophysical and Laboratory-Based Data: An Example. *Surveys in Geophysics* 37, 149–189. doi:10.1007/s10712-015-9353-z.
- Kim, T., O'Rourke, J.G., Lee, J., Chariton, S., Prakapenka, V., Husband, R.J., Giordano, N., Liermann, H.P., Shim, S.H., Lee, Y., 2023. A hydrogen-enriched layer in the topmost outer core sourced from deeply subducted water. *Nature Geoscience* 16, 1208–1214. doi:10.1038/s41561-023-01324-x.
- Kiseeva, E.S., Vasiukov, D.M., Wood, B.J., McCammon, C., Stachel, T., Bykov, M., Bykova, E., Chumakov, A., Cerantola, V., Harris, J.W., Dubrovinsky, L., 2018. Oxidized iron in garnets from the mantle transition zone. *Nature Geoscience* 11, 144–147. doi:10.1038/s41561-017-0055-7.
- Kohlstedt, D.L., Mackwell, S.J., 1998. Diffusion of Hydrogen and Intrinsic Point Defects in Olivine. *Zeitschrift für Physikalische Chemie* 207, 147–162. doi:10.1524/zpch.1998.207.part\_1\_2.147.
- Liu, H., Yang, X., 2020. Solubility of hydroxyl groups in pyroxenes: Effect of oxygen fugacity at 0.2–3 GPa and 800–1200 °C. *Geochimica et Cosmochimica Acta* 286, 355–379. doi:10.1016/j.gca.2020.07.034.
- Liu, Z., Fei, H., Chen, L., McCammon, C., Wang, L., Liu, R., Wang, F., Liu, B., Katsura, T., 2021. Bridgmanite is nearly dry at the top of the lower mantle. *Earth and Planetary Science Letters* 570, 117088. doi:10.1016/j.epsl.2021.117088.
- Lu, W., Yang, Y.N., Long, T., Xian, H., Li, Y., Du, Z., 2025. Substantial water retained early in Earth's deep mantle. *Science* 390, 1177–1180. doi:10.1126/science.adx5883.
- McCammon, C., 2005a. The Paradox of Mantle Redox. *Science* 308, 807–808. doi:10.1126/science.1110532.
- McCammon, C., Frost, D., Smyth, J., Laustsen, H., Kawamoto, T., Ross, N., Van Aken, P., 2004. Oxidation state of iron in hydrous mantle phases: implications for subduction and mantle oxygen fugacity. *Physics of the Earth and Planetary Interiors* 143-144, 157–169. doi:10.1016/j.pepi.2003.08.009.

- McCammon, C.A., 2005b. Mantle oxidation state and oxygen fugacity: Constraints on mantle chemistry, structure, and dynamics, in: Van Der Hilst, R.D., Bass, J.D., Matas, J., Trampert, J. (Eds.), *Geophysical Monograph Series*. American Geophysical Union, Washington, D. C.. volume 160, pp. 219–240. doi:10.1029/160GM14.
- Miller, W.G.R., Holland, T.J.B., Gibson, S.A., 2016. Garnet and Spinel Oxybarometers: New Internally Consistent Multi-equilibria Models with Applications to the Oxidation State of the Lithospheric Mantle. *Journal of Petrology* 57, 1199–1222. doi:10.1093/petrology/egw037.
- Moine, B.N., Bolfan-Casanova, N., Radu, I.B., Ionov, D.A., Costin, G., Korsakov, A.V., Golovin, A.V., Oleinikov, O.B., Delouie, E., Cottin, J.Y., 2020. Molecular hydrogen in minerals as a clue to interpret  $\delta D$  variations in the mantle. *Nature Communications* 11, 3604. doi:10.1038/s41467-020-17442-8.
- Muir, J.M., Brodholt, J.P., 2018. Water distribution in the lower mantle: Implications for hydrolytic weakening. *Earth and Planetary Science Letters* 484, 363–369. doi:10.1016/j.epsl.2017.11.051.
- Okuchi, T., 1997. Hydrogen Partitioning into Molten Iron at High Pressure: Implications for Earth's Core. *Science* 278, 1781–1784. doi:10.1126/science.278.5344.1781.
- Otsuka, K., Karato, S.i., 2012. Deep penetration of molten iron into the mantle caused by a morphological instability. *Nature* 492, 243–246. doi:10.1038/nature11663.
- Panero, W.R., Pigott, J.S., Reaman, D.M., Kabbes, J.E., Liu, Z., 2015. Dry (Mg,Fe)SiO<sub>3</sub> perovskite in the Earth's lower mantle. *Journal of Geophysical Research: Solid Earth* 120, 894–908. doi:10.1002/2014JB011397.
- Peltier, W.R., 1985. New constraints on transient lower mantle rheology and internal mantle buoyancy from glacial rebound data. *Nature* 318, 614–617. doi:10.1038/318614a0.
- Piet, H., Badro, J., Nabiei, F., Dennenwaldt, T., Shim, S.H., Cantoni, M., Hébert, C., Gillet, P., 2016. Spin and valence dependence of iron partitioning in Earth's deep mantle. *Proceedings of the National Academy of Sciences* 113, 11127–11130. doi:10.1073/pnas.1605290113.
- Rohrbach, A., Ballhaus, C., Golla-Schindler, U., Ulmer, P., Kamenetsky, V.S., Kuzmin, D.V., 2007. Metal saturation in the upper mantle. *Nature* 449, 456–458. doi:10.1038/nature06183.
- Shibazaki, Y., Ohtani, E., Terasaki, H., Suzuki, A., Funakoshi, K.i., 2009. Hydrogen partitioning between iron and ringwoodite: Implications for water transport into the Martian core. *Earth and Planetary Science Letters* 287, 463–470. doi:10.1016/j.epsl.2009.08.034.
- Stagno, V., Tange, Y., Miyajima, N., McCammon, C.A., Irifune, T., Frost, D.J., 2011. The stability of magnesite in the transition zone and the lower mantle as function of oxygen fugacity: CARBON/CARBONATE fo2 BUFFER AT HP. *Geophysical Research Letters* 38, n/a–n/a. doi:10.1029/2011GL049560.
- Stixrude, L., Lithgow-Bertelloni, C., 2005. Thermodynamics of mantle minerals - I. Physical properties. *Geophysical Journal International* 162, 610–632. doi:10.1111/j.1365-246X.2005.02642.x.

- Stixrude, L., Lithgow-Bertelloni, C., 2011. Thermodynamics of mantle minerals - II. Phase equilibria. *Geophysical Journal International* 184, 1180–1213. doi:10.1111/j.1365-246X.2010.04890.x.
- Stixrude, L., Lithgow-Bertelloni, C., 2024a. HeFESTo: Helmholtz Free Energy Self-consistent Thermodynamics. URL: <https://github.com/stixrude/HeFESToRepository>; [https://github.com/stixrude/HeFESTo\\_Parameters\\_010123](https://github.com/stixrude/HeFESTo_Parameters_010123).
- Stixrude, L., Lithgow-Bertelloni, C., 2024b. Thermodynamics of mantle minerals – III: The role of iron. *Geophysical Journal International* 237, 1699–1733. doi:10.1093/gji/ggae126.
- Stoutenburg, E.R., Caracas, R., Campbell, A.J., 2026. Immiscibility between hydrogen and molten iron in planetary cores. *Earth and Planetary Science Letters* 678, 119851. doi:10.1016/j.epsl.2026.119851.
- Wang, F., Fei, H., Wang, L., McCammon, C., Frost, D.J., Katsura, T., 2023. A decrease in the  $\text{Fe}^{3+}/\Sigma\text{Fe}$  ratio of bridgmanite with temperature at the top of the lower mantle. *Earth and Planetary Science Letters* 624, 118440. doi:10.1016/j.epsl.2023.118440.
- Wang, F., Wang, L., Fei, H., Miyajima, N., McCammon, C., Frost, D.J., Katsura, T., 2025. Bridgmanite's ferric iron content determined Earth's oxidation state. *Nature Geoscience* doi:10.1038/s41561-025-01725-0.
- Workman, R.K., Hart, S.R., 2005. Major and trace element composition of the depleted MORB mantle (DMM). *Earth and Planetary Science Letters* 231, 53–72. doi:10.1016/j.epsl.2004.12.005.
- Yagi, T., Hishinuma, T., 1995. Iron hydride formed by the reaction of iron, silicate, and water: Implications for the light element of the Earth's core. *Geophysical Research Letters* 22, 1933–1936. doi:10.1029/95GL01792.
- Yang, X., 2016. Effect of oxygen fugacity on OH dissolution in olivine under peridotite-saturated conditions: An experimental study at 1.5–7 GPa and 1100–1300 °C. *Geochimica et Cosmochimica Acta* 173, 319–336. doi:10.1016/j.gca.2015.11.007.
- Yang, X., Keppler, H., Li, Y., 2016. Molecular hydrogen in mantle minerals. *Geochemical Perspectives Letters*, 160–168 doi:10.7185/geochemlet.1616.
- Yuan, H., Zhang, L., Ohtani, E., Meng, Y., Greenberg, E., Prakapenka, V.B., 2019. Stability of Fe-bearing hydrous phases and element partitioning in the system  $\text{MgO-Al}_2\text{O}_3\text{-Fe}_2\text{O}_3\text{-SiO}_2\text{-H}_2\text{O}$  in Earth's lowermost mantle. *Earth and Planetary Science Letters* 524, 115714. doi:10.1016/j.epsl.2019.115714.
- Yuan, L., Ohtani, E., Ikuta, D., Kamada, S., Tsuchiya, J., Naohisa, H., Ohishi, Y., Suzuki, A., 2018. Chemical Reactions Between Fe and  $\text{H}_2\text{O}$  up to Megabar Pressures and Implications for Water Storage in the Earth's Mantle and Core. *Geophysical Research Letters* 45, 1330–1338. doi:10.1002/2017GL075720.
- Zhang, L., Chen, Y., Yang, Z., Liu, L., Yang, Y., Dalladay-Simpson, P., Wang, J., Mao, H.k., 2024. Pressure stabilizes ferrous iron in bridgmanite under hydrous deep lower mantle conditions. *Nature Communications* 15, 4333. doi:10.1038/s41467-024-48665-8.

- Zhang, Z., Dorfman, S.M., Labidi, J., Zhang, S., Li, M., Manga, M., Stixrude, L., McDonough, W.F., Williams, Q., 2016. Primordial metallic melt in the deep mantle. *Geophysical Research Letters* 43, 3693–3699. doi:10.1002/2016GL068560.
- Zhu, F., Lai, X., Jiang, Y., Chen, B., Chariton, S., Prakapenka, V., Wu, X., 2025a. Deep Hydrogen Cycle Facilitated by Redox Dehydrogenation and Hydration. *Geophysical Research Letters*, e2025GL115820.
- Zhu, F., Li, J., Liu, J., Dong, J., Liu, Z., 2019. Metallic iron limits silicate hydration in Earth's transition zone. *Proceedings of the National Academy of Sciences* 116, 22526–22530. doi:10.1073/pnas.1908716116.
- Zhu, J., Tao, R., Ishii, T., Ikuta, D., Xu, W., Zhang, L., Su, Y., Liu, R., Jin, Z., 2025b. Iron hydride (FeH<sub>x</sub>) as a crucial intermediate in transformation of subducted H<sub>2</sub>O to abiotic H<sub>2</sub> in Earth's deep mantle. *Science China Earth Sciences* 68, 1485–1496. doi:10.1007/s11430-024-1544-6.

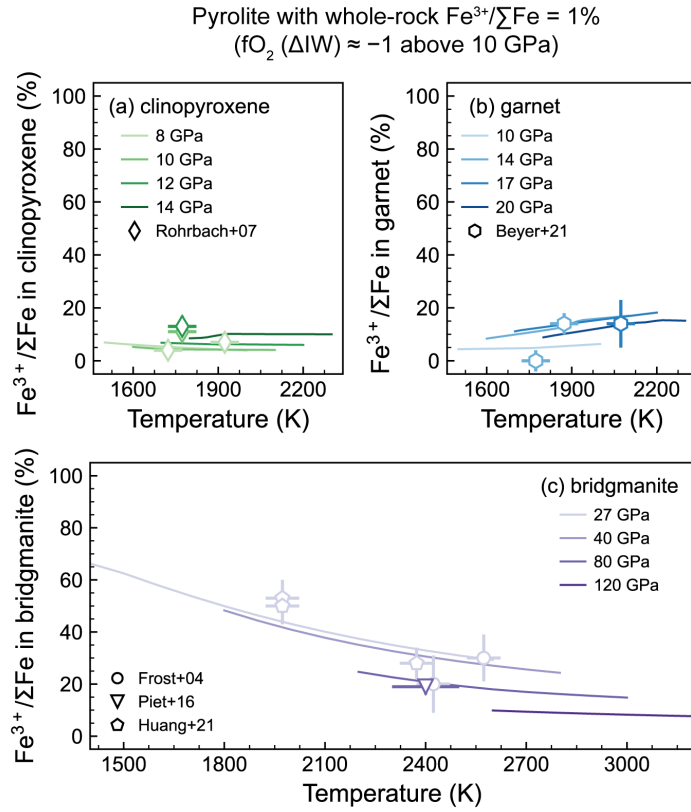


Figure 1: **Predicted ferric content in mantle minerals within pyrolite at whole-rock  $\text{Fe}^{3+}/\Sigma\text{Fe} = 1\%$ , benchmarked against experimental data collected under similarly reduced conditions.** This composition represents a reduced endmember of Earth’s mantle, in which metal saturation is present at all depths above 10 GPa with  $f\text{O}_2(\Delta\text{IW}) \approx -1$ . (a) Ferric content in clinopyroxene show negligible temperature dependence but increases slightly with pressure across 8–14 GPa; experimental data from Rohrbach et al. (2007) (diamond) are shown for comparison. (b) Garnet shows a subtle positive temperature effect on its ferric content and a reversed pressure effect: ferric iron increases up to about 17 GPa before decreasing at 20 GPa, in alignment with the experimental data of Beyer et al. (2021). (c) Ferric iron in brigmanite shows both negative temperature and pressure effects from 27 to 120 GPa, consistent with experimental data from Frost et al. (2004); Huang et al. (2021a), and a reinterpreted data point from Piet et al. (2016). This reinterpreted data of Piet et al. (2016) (at about 86 GPa and about 2400 K) is included as an upper bound for the reduced pyrolite (at whole-rock  $\text{Fe}^{3+}/\Sigma\text{Fe} = 1\%$  and  $f\text{O}_2(\Delta\text{IW}) \approx -1$ ). The negative pressure and temperature effects shown here align well with prior thermodynamic predictions of pressure dependence, which use independent choices of equation of state (Huang et al., 2021b), and recent experimental data to systematically constrain the temperature effect up to 2600 K (Wang et al., 2023) and pressure effect up to 50 GPa (Wang et al., 2025). See Section 3.1 for details.

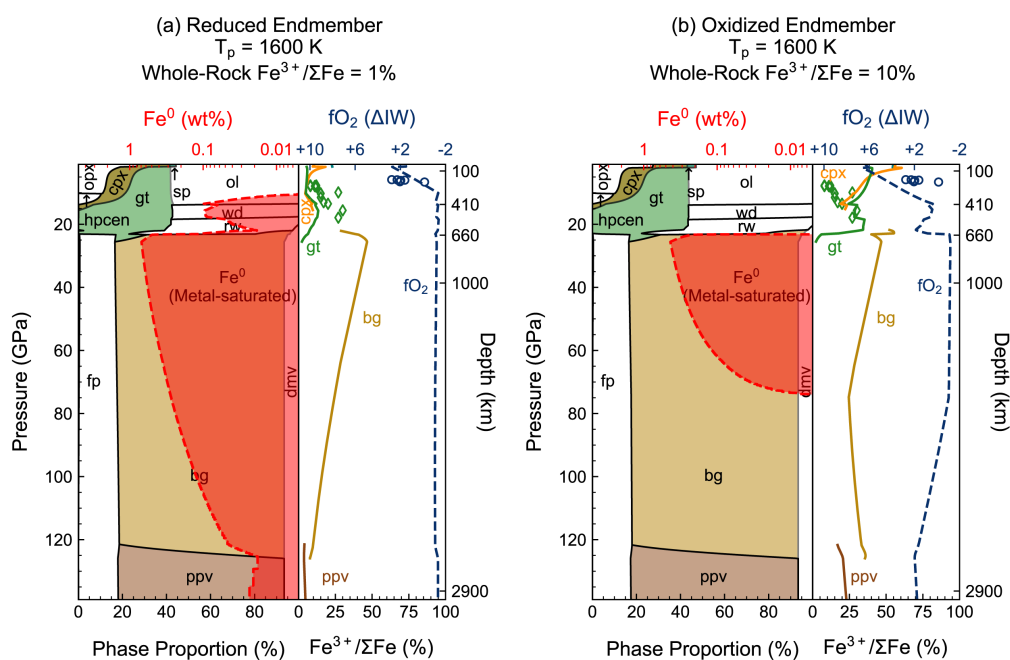


Figure 2: **Distribution of metallic  $\text{Fe}^0$  in the present-day mantle ( $T_p = 1600 \text{ K}$ ) for the reduced (1%, a) and oxidized (10%, b) endmembers.** (a) In the reduced endmember, metal saturation begins in the upper mantle, and  $\text{Fe}^0$  abundance decreases with depth as metal production from bridgmanite becomes less favorable at higher pressure. (b) In the oxidized endmember, metal saturation is confined to the upper- and mid-lower mantle and disappears above approximately 80 GPa as Fe is resorbed into mantle rocks. The contrast highlights how bulk mantle oxidation state (indicated by whole-rock  $\text{Fe}^{3+}/\Sigma\text{Fe}$ ) controls both the depth and stability of  $\text{Fe}^0$  in the present-day Earth's mantle ( $T_p = 1600 \text{ K}$ ). Left panels show phase abundances as a function of depth, with mantle phases labeled (spinel = sp, orthopyroxene = opx, clinopyroxene = cpx, high-pressure clinopyroxene/olivine = hpcen, olivine = ol, wadsleyite = wd, ringwoodite = rw, bridgmanite = bg, ferropericlasite = fp, davemaolite = dmv, post-perovskite = ppv). The lower x-axis gives cumulative phase proportions, with the red dashed line marking disproportionated metal; the upper x-axis shows the metal fraction on a logarithmic scale. Right panels show mantle oxygen fugacity  $f\text{O}_2$  (navy dashed line) and ferric iron contents in individual minerals (colored lines). The lower x-axis gives the ferric iron content as a percentage of total iron in each phase, while the upper x-axis shows  $f\text{O}_2$  normalized to the iron-wüstite (IW) buffer on a reversed logarithmic scale.

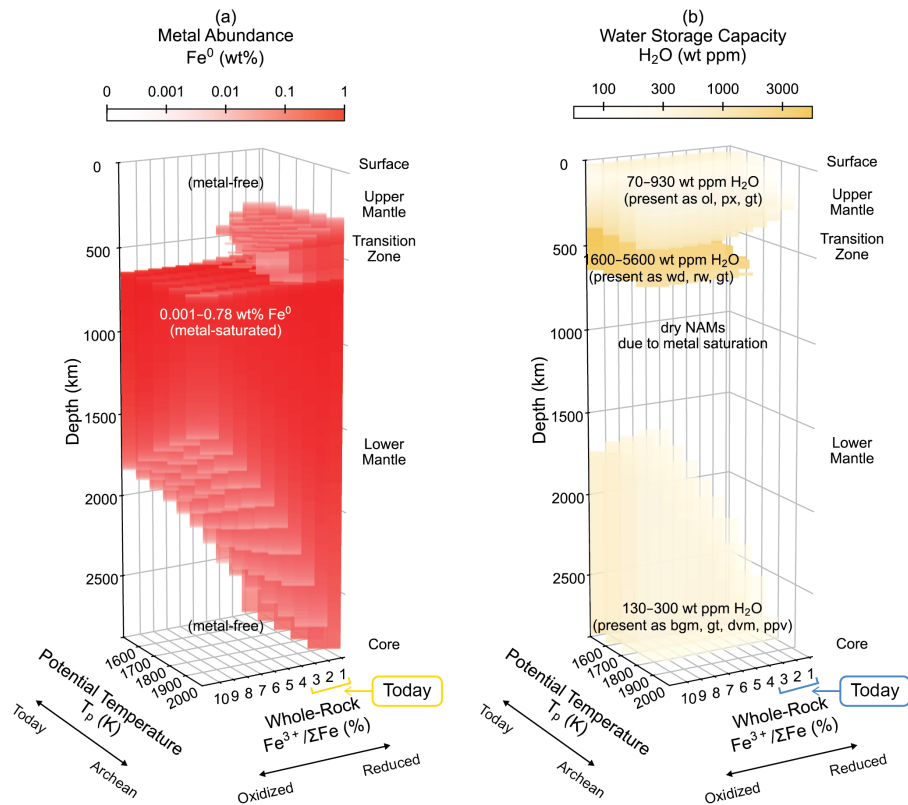


Figure 3: **Widespread metal saturation destabilizes structural OH in NAMs, resulting in a dry deep mantle.** Distribution of metal abundance (a) and water storage capacity (b) in Earth's mantle are modeled as functions of depth (km), potential temperature  $T_p$  (K), and oxidation state, expressed as the whole-rock  $Fe^{3+}/\Sigma Fe$  ratio (%). Present-day whole-rock  $Fe^{3+}/\Sigma Fe = 1\text{--}3\%$  yields persistent metal saturation from the upper to lowermost mantle, with  $Fe^0$  reaching up to 0.78 wt% in (a). More oxidized bulk compositions ( $>3\%$ ) confine metal saturation to the upper- and mid-lower mantle. NAMs in (b) can store up to 930 ppm  $H_2O$  by weight in the upper mantle, but transition-zone hydration is likely suppressed because metal saturation has been attained today with the whole-rock  $Fe^{3+}/\Sigma Fe$  range of 1–3%. In contrast, in much more oxidized bulk compositions (6–10%), NAMs can retain up to 5600 ppm  $H_2O$ ; in the lowermost mantle (80–120 GPa), resorption of metal may once again permit a moderate  $H_2O$  storage capacity of 130–300 ppm.

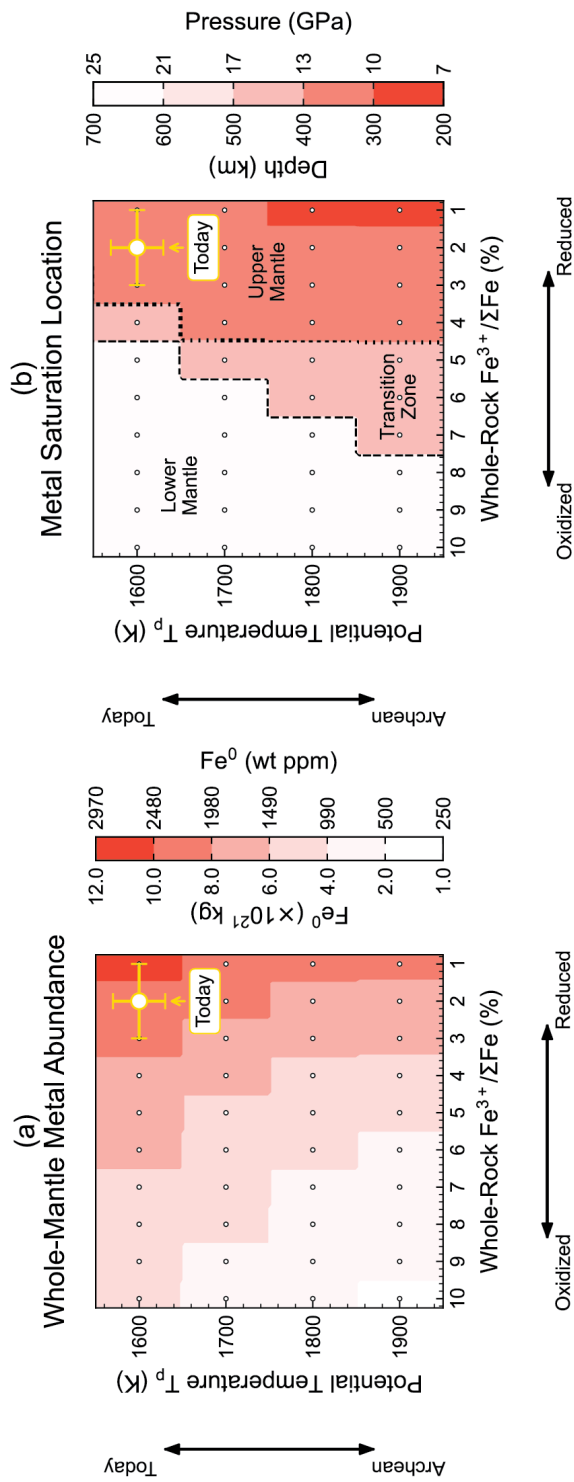


Figure 4: **Metallic  $Fe^0$  amounts to  $8.6\text{--}10.5 \times 10^{21}$  kg (2120–2600 ppm by weight) in Earth's mantle today, stabilizing near the base of the upper mantle and extending to the core-mantle boundary.** Whole-mantle metallic  $Fe^0$  abundance (a) and saturation depth (b) are modeled as functions of potential temperature  $T_p$  (K) and oxidation state, expressed as the whole-rock  $Fe^{3+}/\Sigma Fe$  ratio (%). Bulk metallic  $Fe^0$  abundance (expressed in wt ppm and kg) increases with decreasing  $T_p$  and with increasing whole-rock  $Fe^{3+}/\Sigma Fe$ . For the present-day range of 1–3%, metal saturation typically begins in the upper mantle (300–400 km). In more oxidized compositions (4–10%), metal saturation is delayed to the transition zone and sometimes confined to the lower mantle. Higher  $T_p$  shifts the onset of metal saturation deeper, even as bulk metallic  $Fe^0$  abundance declines.

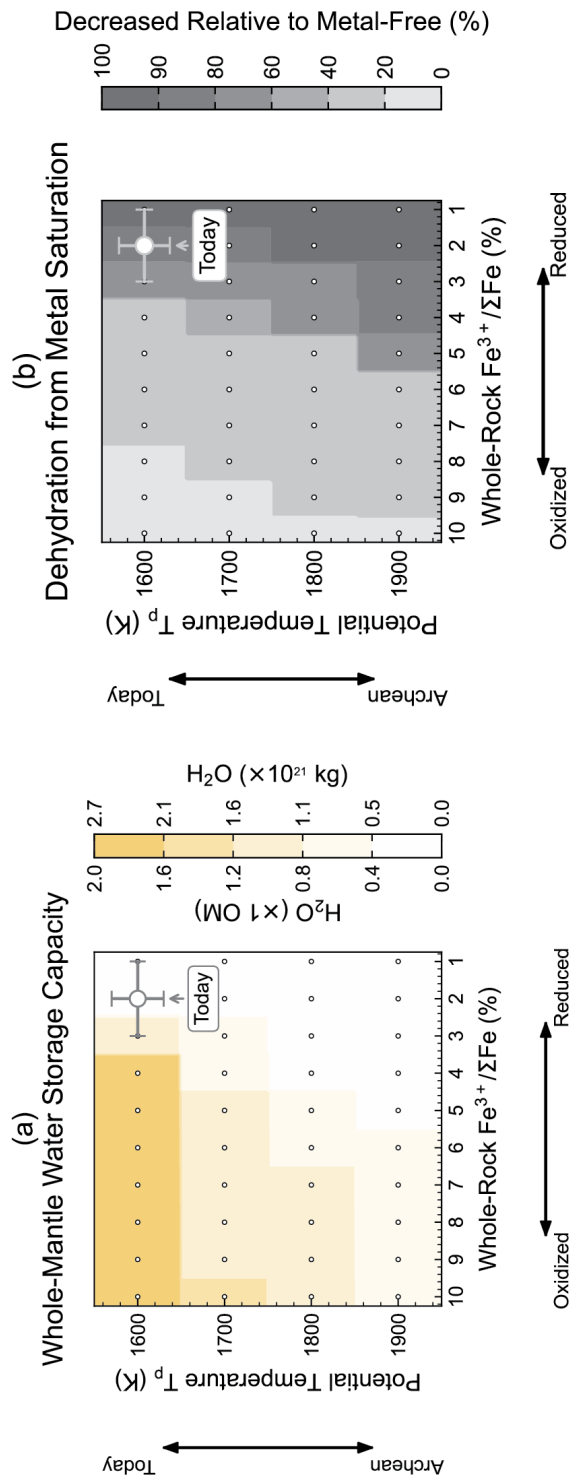


Figure 5: **Whole-mantle water storage capacity falls by 64–96% today, from 2.3 to 0.1–0.8 modern ocean masses, when metal saturation is taken into account.** Whole-mantle water storage capacity with metal saturation (this work, a) are modeled as functions of potential temperature  $T_p$  (K) and oxidation state, expressed as the whole-rock  $\text{Fe}^{3+}/\Sigma\text{Fe}$  ratio (%), and its decrease relative to metal-free models (b, Dong et al., 2021). Whole-mantle water storage capacity (expressed in kg and modern ocean mass, OM) increases with decreasing  $T_p$  and with increasing whole-rock  $\text{Fe}^{3+}/\Sigma\text{Fe}$ . For the present-day range of 1–3%, whole-mantle storage capacity ( $T_p = 1600$  K) is reduced by 64–96% due to metal saturation, from nearly  $3.00 \times 10^{21}$  kg (2.3 OM, Dong et al. (2021)) to  $0.12\text{--}1.08 \times 10^{21}$  kg (0.1–0.8 OM, this work). In more oxidized compositions (4–10%), present-day storage capacity has a more modest decrease relative to metal-free models (18–27%). The larger drops in storage capacity occur when lower whole-rock  $\text{Fe}^{3+}/\Sigma\text{Fe}$  and higher  $T_p$  enable metal saturation in the transition zone, where silicates would otherwise have the highest intrinsic water storage capacity under metal-free conditions.